Anisotropic inversion and imaging of *PP* and *PS* reflection data in the North Sea

VLADIMIR GRECHKA, *Shell International Exploration and Production, Houston, Texas, U.S.*
ILYA TSVANKIN, *Colorado School of Mines, Golden, Colorado, U.S.*
ANDREY BAKULIN *and* CLAUDE SIGNER, *Schlumberger Cambridge Research, Cambridge, U.K.*
JAN OVE HANSEN, *Statoil, Harstad, Norway*

The technology of ocean-bottom surveys has put mode-converted waves at the forefront of seismic exploration and reservoir characterization. For example, *PS*-waves proved effective in imaging offshore reservoirs screened by gas clouds that cause high attenuation/scattering of compressional energy (e.g., Thomsen, 1999). Also, information about shear-wave velocities contained in converted modes can be used to separate the effects of saturation and pressure and reduce uncertainty in predicting lithology and fluid saturation. The high sensitivity of *PS*-wave reflection coefficients to shear-wave velocity and density makes converted-wave AVO analysis potentially powerful for detecting hydrocarbon-saturated rocks.

Conventional (isotropic) processing of mode conversions, however, often is inadequate because the influence of anisotropy on *PS*-wave moveout and amplitude is much more substantial than that on *P*-wave signatures. In particular, mis-ties between *PP* and *PS* sections (such as different depths of reflectors) are difficult to remove without taking anisotropy into account. Assuming a purely isotropic overburden often causes smearing of the conversion point, which leads to errors in building common-conversion-point (CCP) gathers and poor focusing of *PS* images. Also, shear-wave splitting in anisotropic media makes it necessary to rotate *PS*-wave displacement components prior to imaging or AVO analysis.

The difficulties in applying isotropic processing techniques to mode conversions underscore the importance of anisotropic velocity analysis of *PS* data. In the presence of anisotropy, it is especially beneficial to combine *PP*- and *PS*-waves in model-building algorithms because a certain subset of the medium parameters influences both *P*- and *S*-wave propagation. For transverse isotropy with a vertical symmetry axis (VTI media), signatures of *P*- and *SV*-waves depend on the *P*-wave vertical velocity V_{P0} and Thomsen parameters ε and δ; additionally, *SV*-wave kinematics is a function of the shear-wave vertical velocity V_{S0}. It should be emphasized that reflection traveltimes of *PP*-waves alone typically are insufficient for resolving individual values of V_{P0}, ε and δ.

Anisotropic velocity analysis of *PP* and *PS* data. It is well known that velocity analysis and inversion of *PS*-waves are complicated by such features as conversion-point dispersal, polarity reversal, and moveout asymmetry with respect to zero offset (i.e., the traveltime of *PS*-waves generally does not remain the same if source and receiver are interchanged). The last problem, called the "diodic velocity" by Thomsen (1999), is the most serious because it precludes application of the conventional hyperbolic moveout equation to converted waves. To overcome the inherent difficulties in dealing with *PS*-waves, Grechka and Tsvankin (2001) suggested a model-independent procedure to reconstruct the traveltimes of pure *SS*-wave reflections from *PP* and *PS* data. Their algorithm for computing *SS* traveltimes is exact and entirely
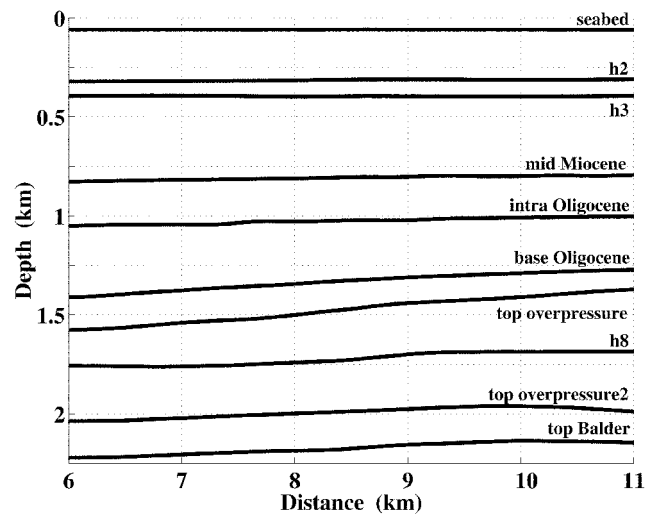

Figure 1. Depth section above Siri reservoir built by Signer et al. (2000).

data-driven, so knowledge of the velocity field is not required. The reconstructed *SS* moveout is symmetric with respect to zero offset and can be processed by velocity-analysis methods developed for pure modes.

An efficient approach to joint inversion of *PP* and *SS* traveltimes is stacking-velocity tomography, which operates with stacking, or normal-moveout (NMO), velocities on 2-D lines and NMO ellipses in wide-azimuth 3-D surveys. For anisotropic models composed of homogeneous layers or blocks separated by smooth interfaces, the NMO ellipse of any pure-mode reflection at a given CMP location can be computed by tracing only one (zero-offset) ray, which makes iterative inversion computationally feasible. Grechka et al. (2001) developed stacking-velocity tomography for multicomponent (*PP* and *SS*) data in TI media with arbitrary tilt of the symmetry axis.

These two new methods provide the basis for the following processing flow devised for anisotropic velocity analysis of multicomponent data:

1) prestack horizon-consistent picking of *PP* and *PS* traveltimes on 2-D or 3-D data volumes and identifying the events reflected from the same interface
2) computation of traveltimes of the pure *SS* reflections from *PP* and *PS* data using the method of Grechka and Tsvankin (2001)
3) tomographic inversion of NMO velocities (in 2-D) or NMO ellipses (in 3-D), zero-offset traveltimes, and reflection slopes for the interval anisotropic parameters (Grechka et al., 2001)

Here we apply this proposed methodology to estimate interval VTI parameters and improve imaging of *PS*-wave data for the Lower Tertiary Siri reservoir in the North Sea.
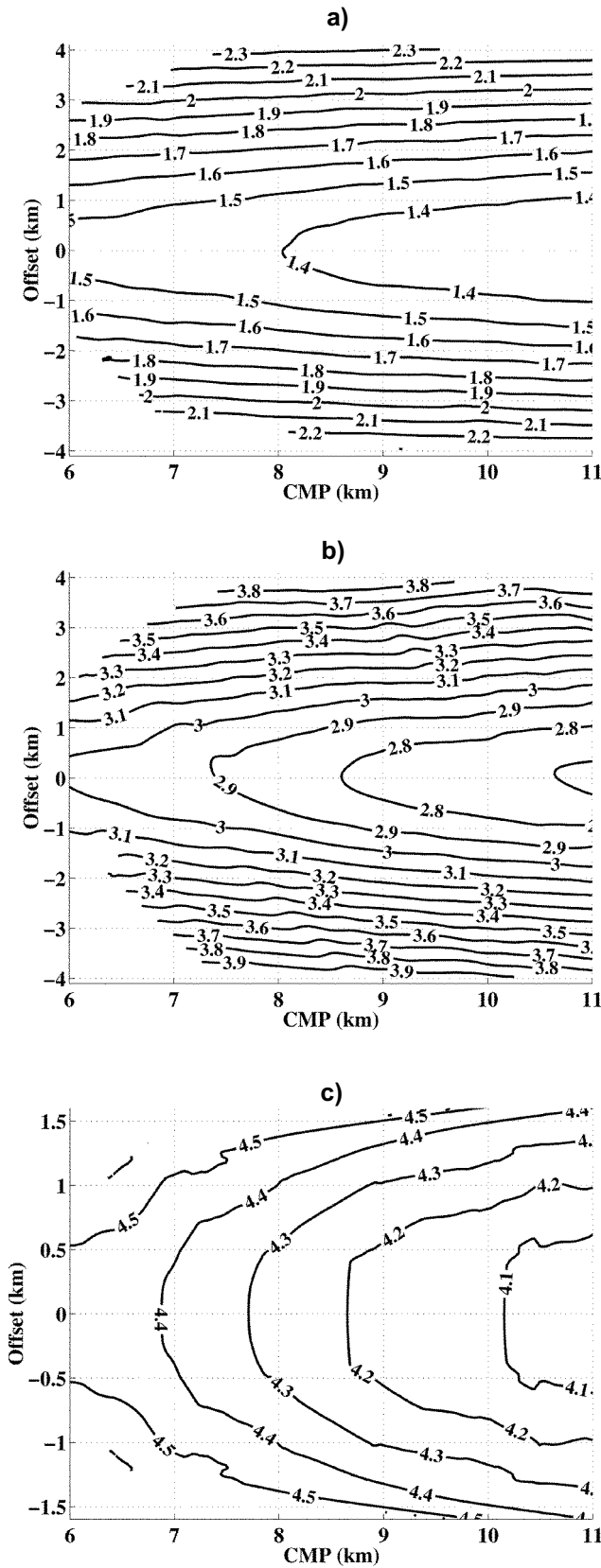
a)

b)

c)

Figure 2. Raw picked traveltimes (in seconds) of the *PP* (a) and *PS* (b) reflections from the top overpressure interface (see Figure 1). (c) *SS*-traveltimes reconstructed from *PP* and *PS* data. Offset *h* (*h* = *r - s*) is either positive or negative, depending on the sign of the difference between the receiver (*r*) and source (*s*) coordinates.

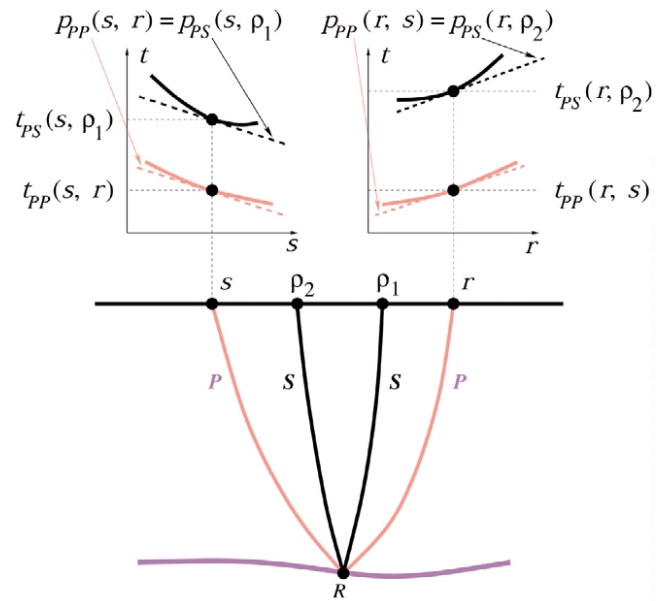Figure 3. Geometry of the *PP* and *PS* reflections from the same interface (in 2-D). p_{PP} (*s*, *r*) and p_{PS} (*s*, ρ_1) are the ray parameters (horizontal slownesses) of the *PP*- and *PS*-waves excited at point *s* and recorded at *r* and ρ_1, respectively (both ray parameters are measured at *s*). p_{PP}(*r*, *s*) and p_{PS}(*r*, ρ_2) are the ray parameters (measured at *r*) of the *PP* - and *PS*-waves excited at *r* and recorded at *s* and ρ_2, respectively. The ray parameters are found as the reflection slopes on common-receiver gathers. Matching the pairs of reflection slopes (ray parameters), p_{PP}(*s*, *r*) = p_{PS} (*s*, ρ_1) and p_{PP}(*r*, *s*) = p_{PS}(*r*, ρ_2), allows us to find the source-receiver coordinates ρ_1 and ρ_2 of the pure *SS* ray with the trajectory $\rho_1 R \rho_2$. The reconstructed *SS*-ray $\rho_1 R \rho_2$ has exactly the same reflection point *R* as the *PP*-ray *sRr* and the *PS*-rays *sR*ρ_1 and *rR*ρ_2.

Reconstruction of *SS* traveltimes above Siri reservoir. The Siri survey includes three 4-C (multicomponent) seabed seismic lines and an 8.7 × 17.6-km 3-D towed-streamer data set that crosses the Norwegian-Danish North Sea border. This work is limited to 2-D processing of the north-south 4-C line. A detailed description of the acquisition, model-based (isotropic) processing and interpretation, and the subsurface geology can be found in Signer et al. (2000). The deepest interpreted horizon (top Balder) is right above the top of the thin (~30 m) reservoir (Figure 1), and the structure of the overburden is close to horizontally layered.

Prestack *PP* and *PS* (*PSV*) reflection traveltimes for all interpreted horizons in Figure 1 were obtained using a semi-automatic Schlumberger picker. The traveltime picks were made on common-receiver gathers with receiver increment Δr = 200 m; the source increment within each gather (Δs) was 25 m. Figures 2a, b show typical raw *PP* and *PS* traveltime picks for one interface in the overburden. Clearly, *PS* moveout is asymmetric with respect to zero offset; this is partly caused by picking errors and the fact that sources are at the ocean surface and receivers are on the sea bottom. This moveout asymmetry, however, is typical of mode conversions for laterally heterogeneous isotropic media or any anisotropic model without a horizontal symmetry plane. The most pronounced asymmetry is in the area of increased lateral variation in the traveltimes (indicative of lateral heterogeneity) near CMP location x_{CMP} = 8 km (Figure 1).

In reconstructing the *SS* traveltimes (Figure 2c) from those of the *PP* and *PS* (*PSV*) reflections, we followed the

a)

b)

c)

d)
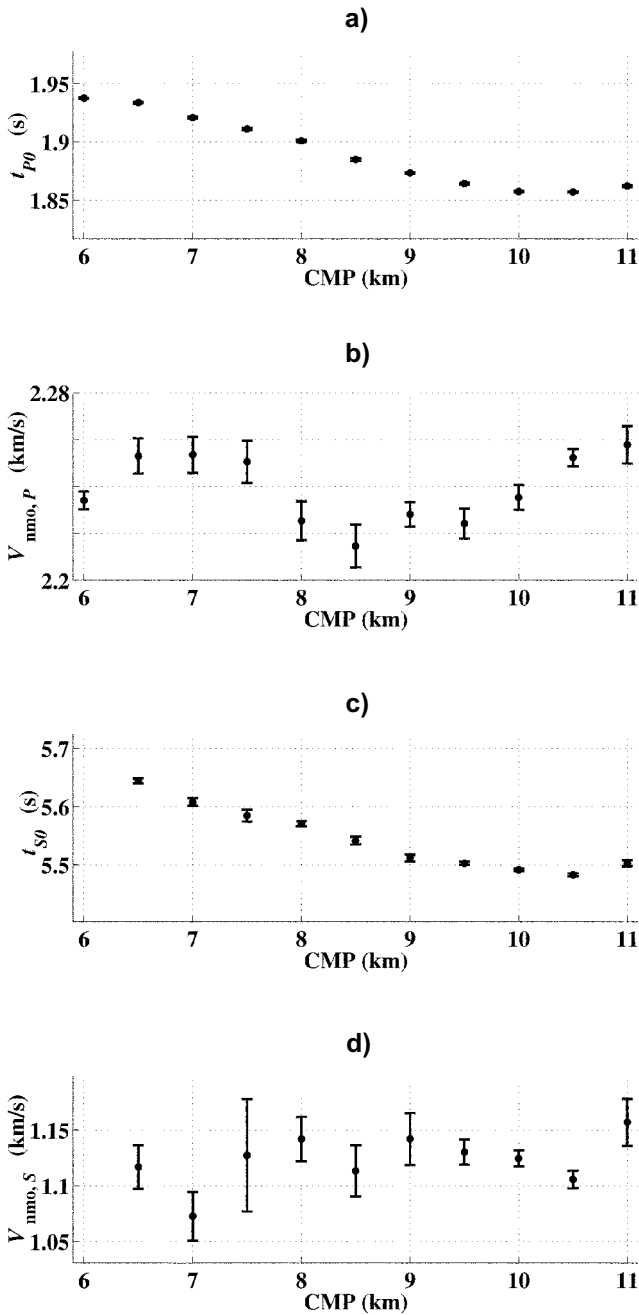
Figure 4. Results of velocity analysis for the top of Balder formation: (a) t_{P0}, (b) $V_{nmo,P}$, (c) t_{S0}, (d) $V_{nmo,S}$. Error bars correspond to 95% confidence intervals.

general methodology of Grechka and Tsvankin (2001). Their algorithm, illustrated in 2-D by Figure 3, is designed to identify receiver coordinates of PP and PS rays that are excited at the same location and have the same reflection point. Then the SS traveltime between obtained shear-wave receiver positions ρ_1 and ρ_2 is

$$t_{SS}\,(\rho_1,\,\rho_2) = t_{PS}\,(s,\rho_1) + t_{PS}\,(r,\,\rho_2) - t_{PP}\,(s,r)\,. \qquad (1)$$

To enforce the symmetry of the SS traveltimes and reduce picking errors, $t_{PP}(s, r)$ was replaced with the average of the reciprocal PP times.

Processing this particular data set required some adjustments because sources and receivers are at different levels. The processing flow to obtain the SS-wave reflection trav-

eltimes from each interface included estimation of reflection slopes (ray parameters) for both PP- and PS-waves at source locations, downward kinematic continuation (mapping) of sources onto the ocean bottom, interpolation of source locations, building common-shot gathers, and matching reflection slopes of PP- and PS-waves at each source location.

Therefore, computation of SS traveltimes is entirely based on recorded reflection data and does not require any information about subsurface velocity or structure. It is assumed, however, that the event-correlation procedure yields PP- and PS-waves reflected from the same interface.

The reconstructed SS-wave traveltimes for the top overpressure interface are shown in Figure 2c. The times in Figures 2a-b were picked for a wide range of offsets limited by $h_{max,PP} \approx h_{max,PS} \approx 4$ km, which yields the maximum offset-to-depth ratio for the top overpressure interface of about 2.5. The offsets of the reconstructed SS reflections are smaller than those for the original PP and PS data ($h_{max,PP}$ has to be divided by the V_P/V_S ratio to estimate the maximum offset for the SS-waves) but still sufficient for moveout velocity analysis.

Velocity analysis of PP and SS data. Traveltimes of PP-waves and reconstructed SS-waves can be used to compute their associated zero-offset times (t_{P0} and t_{S0}) and stacking (moveout) velocities ($V_{nmo,P}$ and $V_{nmo,S}$). To increase fold of SS data, we formed composite CMP gathers that include offset-traveltime pairs from all CMP locations within a certain interval (w_{CMP}). We found that $w_{CMP} = 0.5$ km provides both sufficient stability and acceptable lateral resolution in estimating stacking velocities.

Figure 4 shows zero-offset traveltimes and stacking (NMO) velocities for the top of Balder formation (i.e., the top of Siri reservoir). SS traveltimes are missing near the beginning of the line where the needed PP and PS traveltime picks were not available. The error bars in Figure 4 correspond to the 95% confidence intervals calculated assuming random (Gaussian) distribution of traveltime picks around the best-fit hyperbolas. Only the most reliable portion of the data for CMP locations from 7 to 10 km was used for parameter estimation.

Before describing parameter-estimation results, we briefly discuss properties of estimated moveout velocities and traveltimes indicative of anisotropy. Velocity analysis for the top Balder horizon (Figure 4) and other interfaces yields the ratio of the NMO velocities $g_{nmo} \equiv V_{nmo,S}/V_{nmo,P}$ that can be compared with the ratio g_0 of the vertical velocities of SS-waves (V_{S0}) and PP-waves (V_{P0})($g_0 \equiv V_{S0}/V_{P0} = t_{P0}/t_{S0}$ assuming horizontal interfaces). Note that all velocities represent effective quantities for a particular reflection event.

Figure 5 shows ratios g_0 and g_{nmo} for several interfaces (see Figure 1). Remarkably, for all reflections in the processing, g_{nmo} (on average ≈ 0.45) turned out consistently and significantly greater than g_0 (≈ 0.3). Because such a large difference cannot be caused by vertical heterogeneity in isotropic media, anisotropy is the only plausible explanation for the deviation of g_{nmo} from g_0.

Assuming for simplicity that the medium above each reflector consists of a single homogeneous VTI layer, we can explain the difference between g_0 and g_{nmo} in terms of anisotropic coefficients ε and δ

$$g_{nmo} \equiv \frac{V_{nmo,S}}{V_{nmo,P}} = \frac{V_{S0}\sqrt{1+2\sigma}}{V_{P0}\sqrt{1+2\delta}} = g_0\frac{\sqrt{1+2\sigma}}{\sqrt{1+2\delta}}, \qquad (2)$$

where $\sigma \equiv (V_{P0}/V_{S0})^2 (\varepsilon\text{-}\delta)$. Substituting our estimates of g_{nmo} = 0.45 and g_0 = 0.3 into equation 2 and linearizing it in ε and δ leads to the relationship $\varepsilon \approx 0.06 + 1.25\,\delta$. Clearly, at least
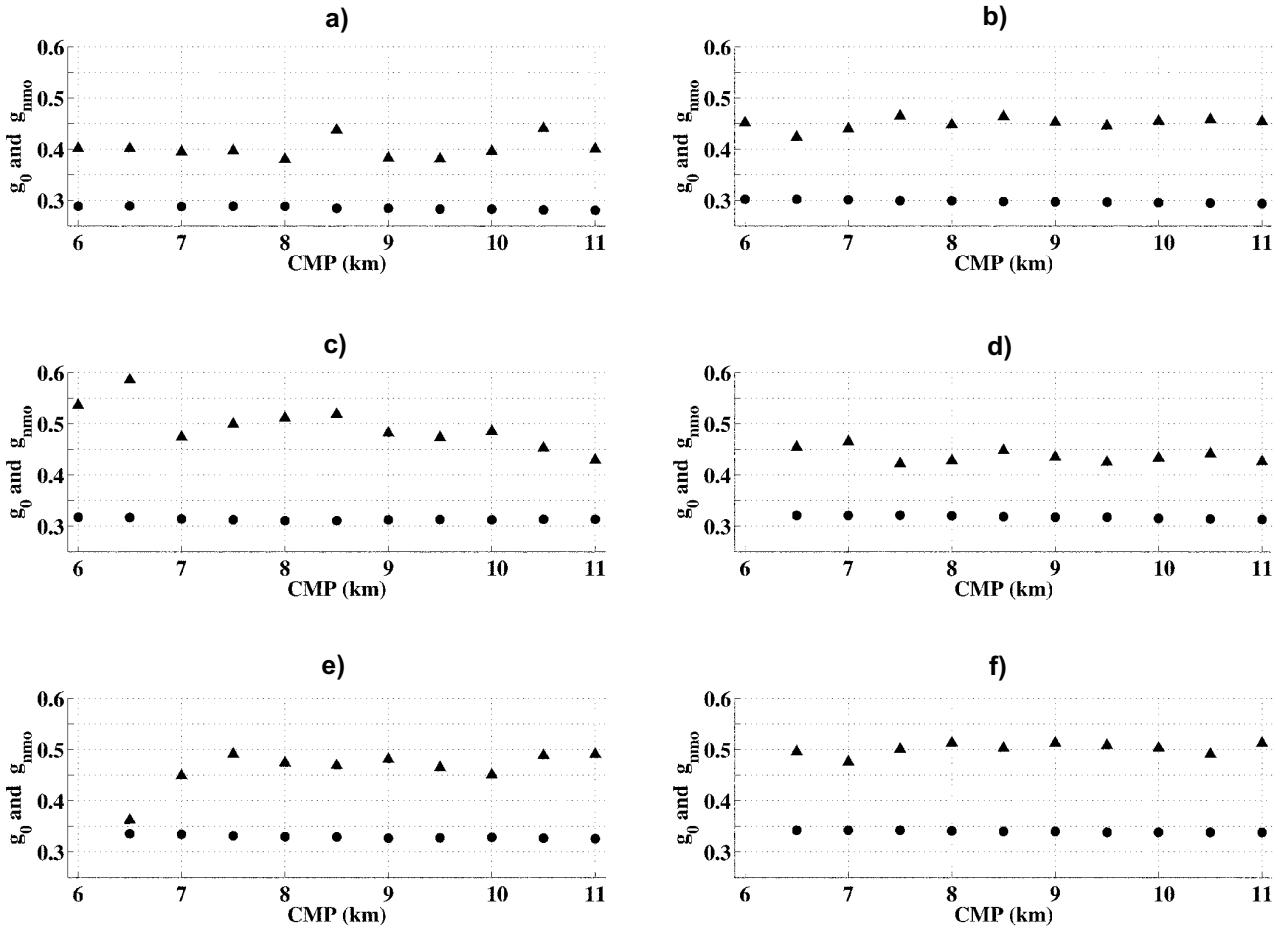
Figure 5. Ratios g_0 (circles) and g_{nmo} (triangles) for the following horizons marked in Figure 1: (a) mid Miocene, (b) intra Oligocene, (c) base Oligocene, (d) top overpressure, (e) h8, and (f) top Balder.

one anisotropic coefficient (ε or δ) does not vanish, and matching of both *PP* and *SS* data requires the subsurface model to be effectively anisotropic.

Estimation of anisotropic parameters. An important prerequisite for successful inversion is identification of the medium parameters constrained by the available data. The low energy recorded on the transverse displacement component (not analyzed here) and the predominantly horizontal layering above the reservoir (Figure 1) suggest that the medium is azimuthally isotropic (i.e., VTI). Because the structure is subhorizontal and assumed to be composed of VTI layers, *PP* and *PS* reflection data can be inverted for NMO velocities and anellipticity parameter η but not for the vertical velocities V_{P0} and V_{S0} and coefficients ε and δ (Tsvankin and Grechka, 2000). In general, *PP* and *PS* reflection traveltimes in horizontally layered VTI media do not constrain reflector depth, even if model parameters are selected in such a way that both *PP* and *PS* common-image gathers are flat and at the same depth. Therefore, in the moveout-inversion procedure described below, δ is set to a certain predetermined value.

Input data included *PP* traveltime picks and reconstructed *SS* traveltimes in the range 7 km $\leq x_{CMP} \leq$ 10 km from the mid-Miocene, intra-Oligocene, base Oligocene, h8, and top Balder horizons. The VTI model in Figure 6 was produced by stacking-velocity tomography for $\delta = 0$ under the assumption that all interfaces are planar and have arbitrary unknown dips. Error bars for interval parameters, corresponding to the 95% confidence intervals, were inferred

from errors in the zero-offset traveltimes and NMO (stacking) velocities, such as those in Figure 4. Setting $\delta = 0.1$ (another plausible value) yields a completely different anisotropic model that fits both *PP* and *PS* data equally well.

With such small reflector dips (Figure 6e), it is possible to assume that all interfaces are horizontal and to apply the conventional Dix formula to obtain interval NMO velocities. Then those velocities can be combined with ratios of interval vertical velocities of *P*- and *S*-waves to estimate interval VTI parameters.

After smoothing the effective NMO velocities, we performed this inversion for CMP locations between 7 and 10 km; as before, δ was fixed to ensure a unique result. Coefficients ε of several equivalent anisotropic models obtained at four CMP locations for a range of δ values are plotted in Figure 7.

All models fit picked *PP* and *PS* traveltimes equally well; the standard deviation between measured and computed traveltimes does not exceed 0.3% for the top Balder reflection. However, it is impossible to find a layered isotropic model that provides a good fit to both *PP* and *PS* data. Although estimated values of ε in each layer do change somewhat along the line, no statistically meaningful lateral variation of ε is observed (the standard deviation of ε for a given δ is about 0.03).

To overcome the inherent nonuniqueness of the inversion of *PP*- and *PS*-wave reflection traveltimes in horizontally layered VTI media, it is necessary to have an independent estimate of at least one model parameter (V_{P0}, V_{S0}, ε, δ, or reflector depth). Here, we combine reflection data

a)

b)

c)

d)

e)
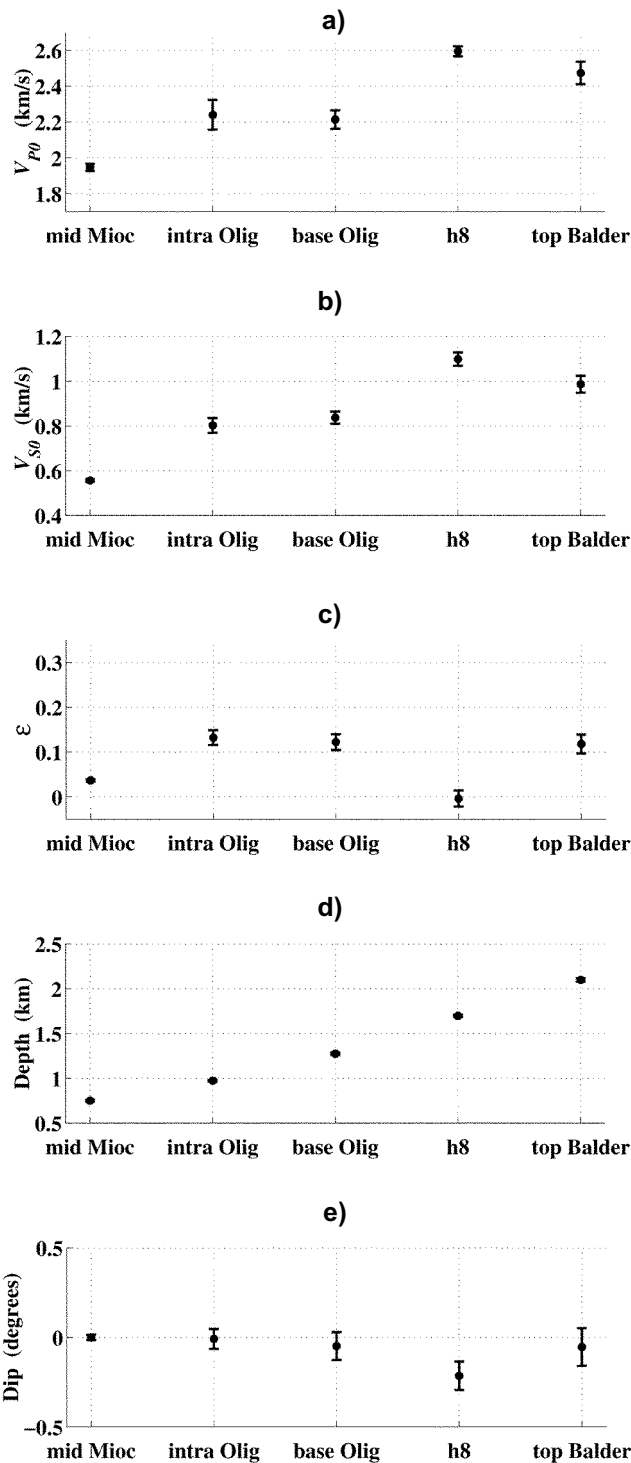
Figure 6. Inverted interval VTI parameters V_{P0} (a), V_{S0} (b), and ε (c) and the reflector depths (d) and dips (e) for CMP locations between 7 and 10 km. Parameter δ = 0 is fixed throughout the section.

with P-wave traveltimes measured using check shots along well Siri-1, which is close to x_{CMP} = 10 km (data courtesy of Statoil). The check shots helped to build the time-to-depth conversion curve and estimate depths of reflectors used in the moveout-inversion algorithm. Then NMO velocities and zero-offset traveltimes of PP- and SS-waves were inverted for VTI parameters V_{P0}, V_{S0}, ε, and δ. The results in Figure 8 were obtained from interval NMO velocities (estimated using the Dix equation) and zero-offset

traveltimes at x_{CMP} = 10 km. Standard deviations in interval values of ε and δ do not exceed 0.03.

The largest interval values of ε and δ are in the middle of the section, with ε reaching almost 0.25 in the Oligocene layer. Clearly, anisotropy is quite significant for both P-waves and, particularly, PS-waves (the interval σ above the reservoir is about 0.5). Also, throughout the section $\varepsilon > \delta$, so parameters η and σ are greater than zero, which is consistent with predominantly positive values of η obtained in other case studies for VTI media (Tsvankin, 2001).

Processing PS data. Because of its model-independent nature, the algorithm of Grechka and Tsvankin (2001) used to reconstruct SS traveltimes is purely kinematic and cannot produce correct reflection amplitudes. Therefore, we processed the original converted-wave data and compared the results obtained for isotropic and VTI models of overburden.

Anisotropic CCP stacks were generated using the inverted VTI model for $\delta = 0$ from Figure 6 (check shots became available after the processing had been completed). Anisotropic traveltime curves and CCP trajectories were computed for each model layer by ray tracing (taking dip into account) and used in CCP stacking. The isotropic model was obtained from the VTI model by setting $\varepsilon = \delta = 0$. Comparing isotropic (Figure 9a) and VTI (Figure 9b) stacked sections reveals significant improvement achieved by accounting for anisotropy. First, application of accurate NMO velocities in the VTI model substantially boosted higher frequencies in the stacked reflections and therefore increased temporal resolution. Second, anisotropic processing provided a crisp picture of faulting in the shallow part of the section and significantly improved the image of the top of the reservoir. Note that although anisotropic parameter estimation was performed only for the left part of the line, improvements are observed for the whole range of CMP locations in Figure 9.

Figures 9c-f help better understand the main reasons for the superior quality of the anisotropic result. As illustrated by Figures 9d and 9e, the correct NMO velocities computed for the VTI model have a much stronger influence on the temporal resolution than on the lateral resolution. To enhance fault imaging, it is necessary to account for anisotropy in computing CCP trajectories (Figures 9d and 9f). Poor focusing and positioning of fault-plane reflections on the isotropic section are explained by the smearing of the conversion point due to anisotropy and layering. We estimated that this smearing at the target level (top Balder) exceeds 500 m for the largest offsets in the data (Figure 10a) and is about 340 m for the maximum offset (2600 m) used to produce the stacks in Figure 9.

Such a significant shift of the conversion point reduces lateral resolution and also biases the isotropic AVO response for PS-waves because each CCP gather includes reflections from a wide range of subsurface points. In addition, neglecting anisotropy in AVO analysis introduces an error in the offset-to-angle transformation that reaches 8° for an offset of 3 km; the corresponding error for PP-waves is only about 2.5° (Figure 10b).

Note that distortions in isotropic processing are particularly severe if PS data are imaged using model-based methods (e.g., Figure 9), including prestack depth migration. Some alternative approaches rely on semblance picking in combination with CCP scanning to find the optimal sorting and to image PS data. Flattening of PS events is often achieved by a moveout equation with parameters that are
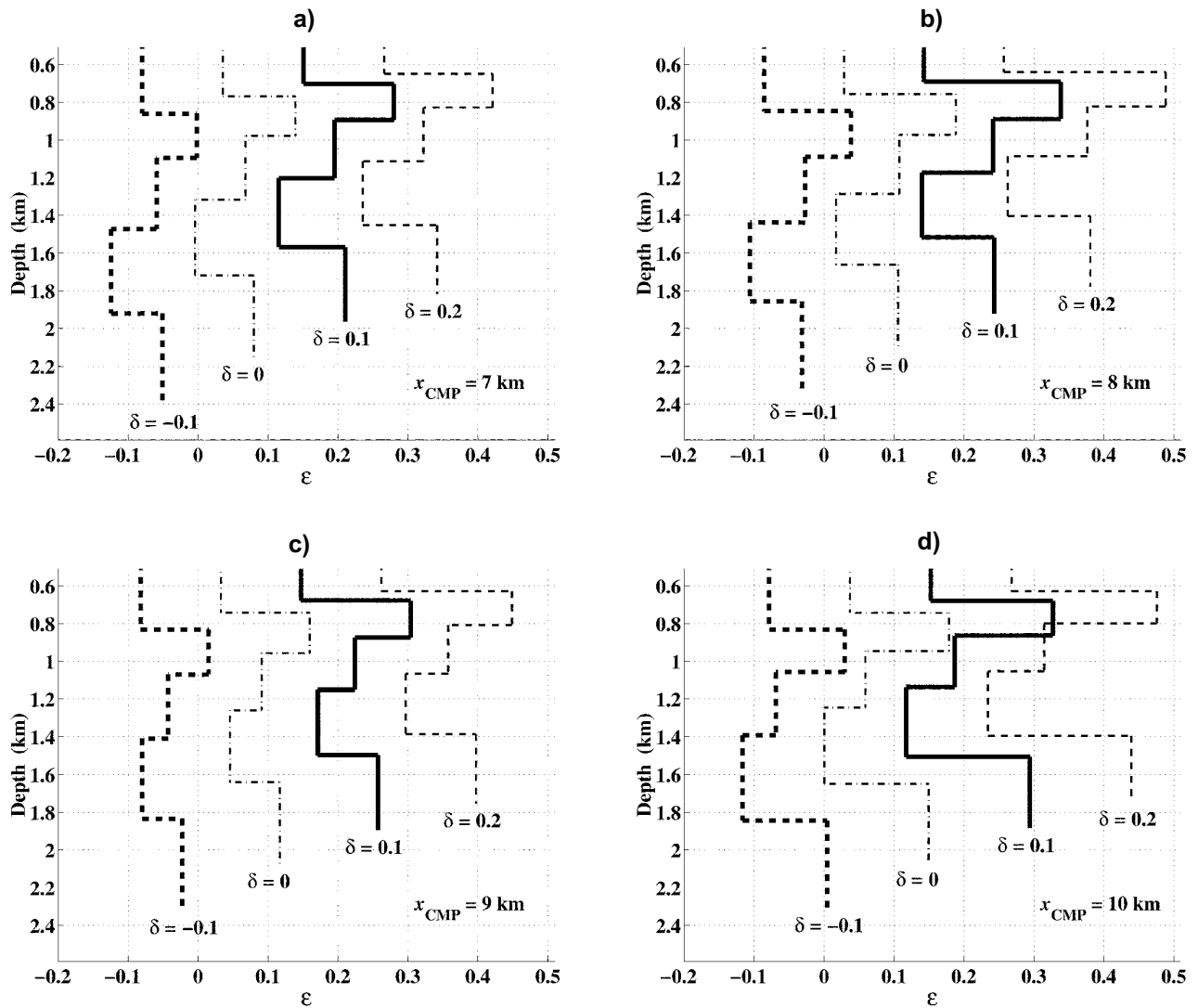
Figure 7. Interval ε estimated for CMP locations (a) 7 km, (b) 8 km, (c) 9 km, and (d) 10 km. Values of δ used to generate ε-curves are marked on the plots.

not derived from the actual subsurface model. To choose the best way of sorting the data, it is possible to analyze imaging results obtained by varying the stacking trajectory and processing positive and negative offsets separately. This method works best if the model has a certain degree of structural complexity; the final trajectory is the one that aligns the structure laterally between the two stacks. Another way of searching for the optimal sorting is based on maximizing semblance in CCP gathers for several key reflectors.

Figure 8. Inversion of reflection and check-shot data at x_{CMP} = 10 km. (a) Interval vertical velocities V_{P0} (solid) and V_{S0} (dashed); (b) interval anisotropic coefficients ε (solid) and δ (dashed).

Although those methods can somewhat improve the quality of the isotropic images in Figure 9, they cannot fully correct the influence of anisotropy. Note that the algorithm outlined in this paper operates on common-receiver gathers and does not depend on the presence of structure, which makes it especially effective for reservoirs in strati-
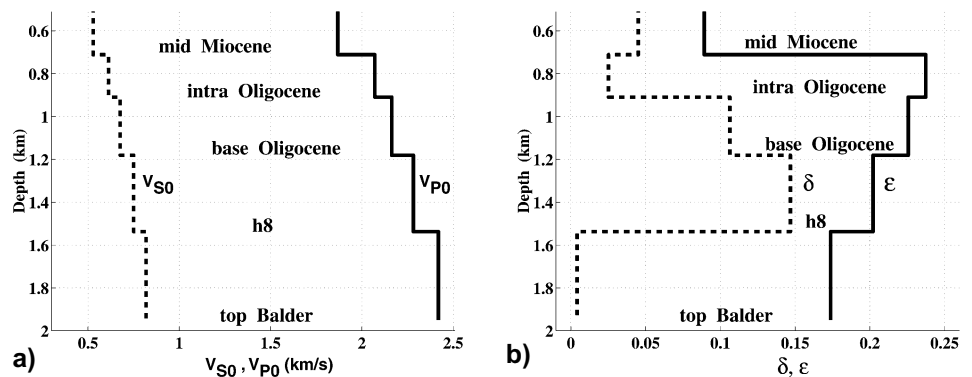
graphic traps. Also, with the advent of prestack depth migration, it becomes necessary to build an accurate physical model of the subsurface that explains all measured signatures simultaneously.

Figure 11 shows time-migrated images of *PS*-waves (a) and *PP*-waves (b) obtained using the VTI velocity model. Although the general appearance of the sections is simi-
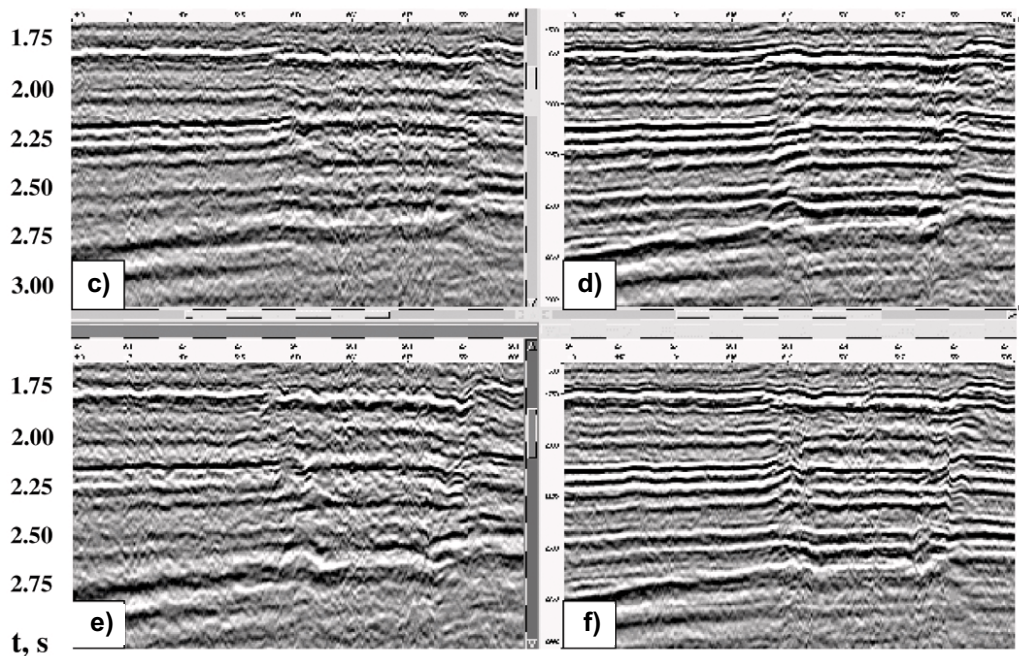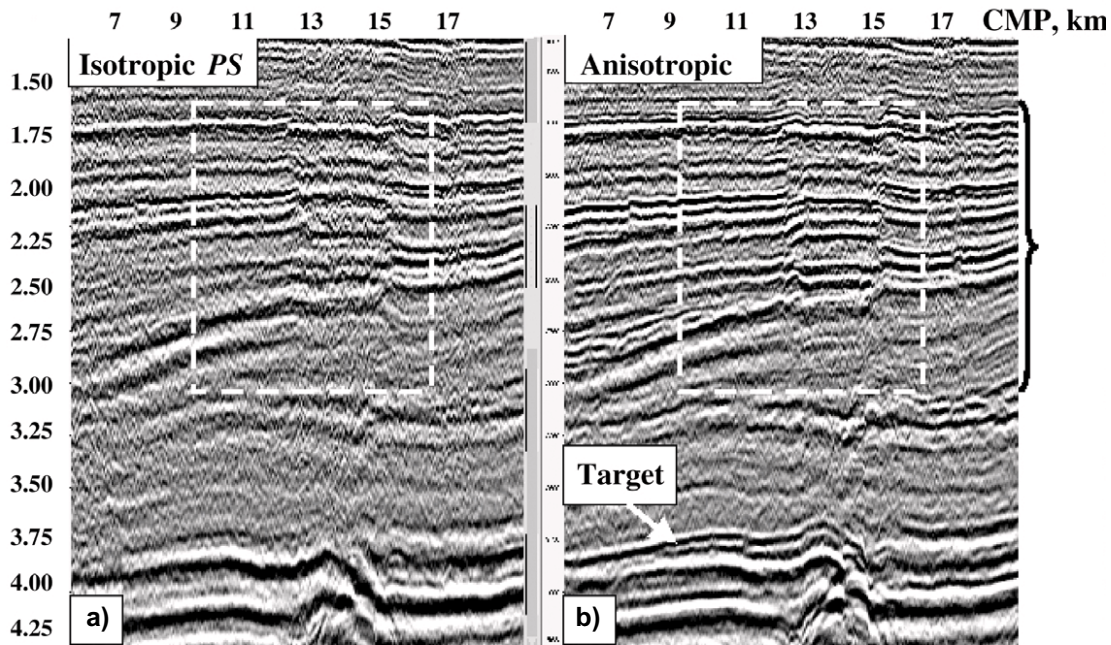
Figure 9. Model-based *PS*-wave common-conversion-point time stacks: (a) isotropic (i.e., corresponding to $\varepsilon = \delta = 0$); (b) VTI. Area marked by the dashed line on plots (a) and (b) obtained with separate moveout computation and CCP sorting: (c) isotropic moveout and isotropic CCP sorting; (d) anisotropic moveout and anisotropic CCP sorting; (e) isotropic moveout and anisotropic CCP sorting; (f) anisotropic moveout and isotropic CCP sorting.

lar, there are some noticeable differences in the images of shallow faults and subhorizontal events at the reservoir level. Because the amplitudes of *PP*- and *PS*-waves depend on different combinations of the medium parameters, *PP* and *PS* images can provide complementary information about the subsurface.

Conclusions. Ignoring seismic anisotropy may cause serious errors in processing and interpretation of multicomponent seismic data, especially if mode-converted *PS*-waves are used for reservoir characterization. This case study shows that overburden anisotropy significantly changes the lateral position of the conversion point, ray trajectories and NMO velocities in CCP gathers, and offset-to-angle mapping. Therefore, assuming isotropy in the overburden severely reduces spatial and temporal resolution of *PS*-wave images and can make them unsuitable for detailed interpretation.
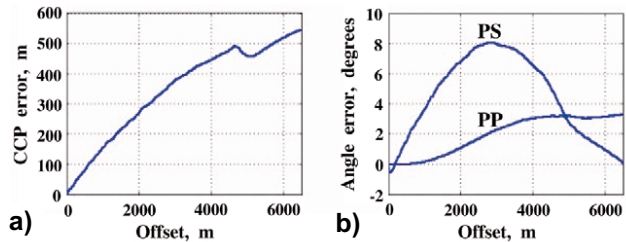

Figure 10. Errors in (a) the lateral position of the *PS*-wave conversion point and (b) the incidence angle of the *P*-leg (for both *PP*- and *PS*-waves) at the target horizon caused by neglecting anisotropy.

We presented a successful application of a methodology designed for anisotropic processing of multicomponent data. The 2-D version of the model-independent algorithm of Grechka and Tsvankin (2001) was used to
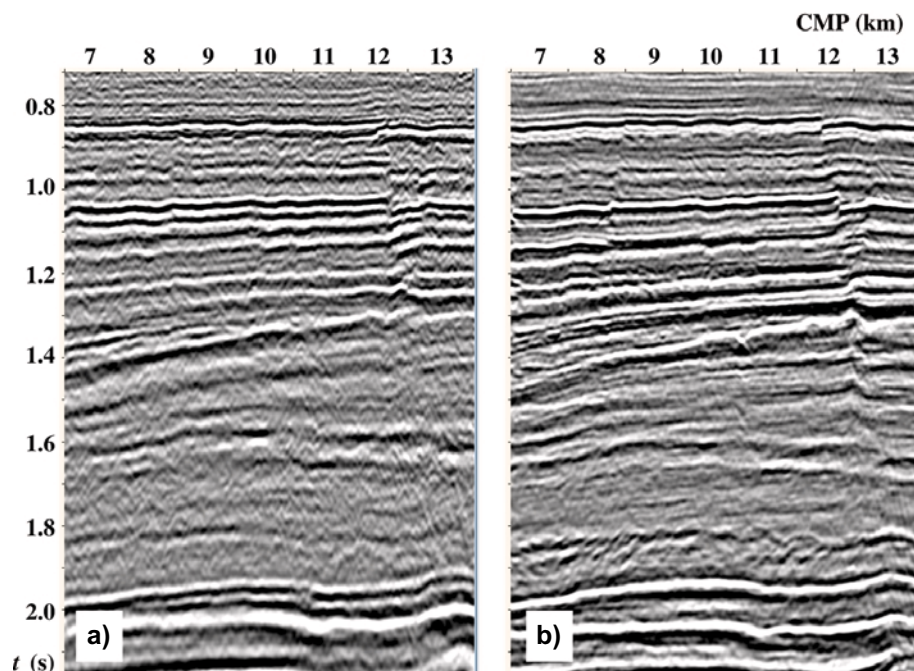
Figure 11. Comparison of time-migrated sections of (a) *PS*-waves and (b) *PP*-waves. The time scale of the *PS* section is compressed by a factor of two. Both sections were computed for the VTI model with $\delta = 0$. The *PS*-wave image is obtained from the CCP stack and the *PP*-wave image from the CRP stack.

reconstruct pure *SS*-wave reflection traveltimes from *PP* and *PS* data. Interval parameters of the assumed VTI model were obtained from joint stacking-velocity tomography of *PP*- and *SS*-waves (Grechka et al., 2001). For horizontally layered VTI media, however, the combination of *PP* and *PS* reflection traveltimes does not constrain the four relevant parameters of VTI media—the *P*- and *S*-wave vertical velocities V_{P0} and V_{S0}, and the anisotropic coefficients ε and δ. Independent information about reflector depths from *P*-wave check shots was used to remove ambiguity in parameter estimation and to build a VTI model suitable for depth imaging.

CCP stacks of *PS*-waves generated for the estimated VTI model have much higher quality than conventional isotropic sections. Most notably, significant improvements were achieved in fault imaging and in the definition of the top of the reservoir. Accounting for anisotropy was also essential for obtaining an accurate AVO response for the *PS* reflections.

Suggested reading. "*PP*+*PS*=*SS*" by Grechka and Tsvankin (2001) and "Multicomponent stacking-velocity tomography for transversely isotropic media" by Grechka, Pech, and Tsvankin (2001), both in SEG's 2001 *Expanded Abstracts*.

"Converted-wave reflection seismology over inhomogeneous, anisotropic media" by Thomsen (GEOPHYSICS, 1999). "Reservoir characterization using 4-C seismic and calibrated 3-D AVO" by Signer et al. (in *Improving the Exploration Process by Learning from the Past*, Elsevier, 2000). "Dip moveout of converted waves and parameter estimation in transversely isotropic media" by Tsvankin and Grechka (*Geophysical Prospecting*, 2000). *Seismic Signatures and Analysis of Reflection Data in Anisotropic Media* by Tsvankin (Elsevier, 2001). A more technical version of the parameter-estimation section of this paper will be published in GEOPHYSICS. Ⅿ

Corresponding author: vladimir.grechka@shell.com, ilya@dix.mines.edu